

---

# CHAPTER 16

---

## AIRBORNE MTI

---

**Fred M. Staudaher**  
*Naval Research Laboratory*

---

### **16.1 SYSTEMS USING AIRBORNE MTI TECHNIQUES**

---

Airborne search radars were initially developed for the detection of ships by long-range patrol aircraft. During the latter part of World War II, airborne early-warning (AEW) radars were developed by the U.S. Navy to detect low-flying aircraft approaching a task force below the radar coverage of the ship's antenna. The advantage of the airborne platform in extending the maximum detection range for air and surface targets is apparent when one considers that the radar horizon is 12 nmi for a 100-ft antenna mast compared with 123 nmi for a 10,000-ft aircraft altitude.

Loss of picket ships due to kamikaze attacks led to the concept of the autonomous airborne detection and control station. This type of system was further developed as a barrier patrol aircraft for continental air defense.

The carrier-based E-2C aircraft (Fig. 16.1) uses AEW radar as the primary sensor in its airborne tactical data system. These radars with their extensive field of view are required to detect small aircraft targets against a background of sea and land clutter. Because of their primary mission of detecting low-flying aircraft, they cannot elevate their antenna beam to eliminate the clutter. These considerations have led to the development of airborne MTI (AMTI)<sup>1-3</sup> radar systems similar to those used in surface radars<sup>1,4-6</sup> discussed in the preceding chapter.

Airborne MTI radar systems have also been utilized to acquire and track targets in interceptor fire control systems. In this application the system has to discriminate against clutter only in the vicinity of a prescribed target. This allows the system to be optimized at the range and angular sector where the target is located. MTI is also used to detect moving ground vehicles by reconnaissance and tactical fighter-bomber aircraft. Because of the low target velocity, higher radar frequencies are employed to obtain a significant doppler shift. Since a strong clutter background is usually present, these systems can effectively utilize noncoherent MTI techniques.

The environment of high platform altitude, mobility, and speed coupled with restrictions on size, weight, and power consumption presents a unique set of



FIG. 16.1 E-2C airborne early-warning (AEW) aircraft showing rotodome housing the antenna.

problems to the designer of airborne MTI systems. This chapter will be devoted to considerations unique to the airborne environment.

## **16.2 COVERAGE CONSIDERATIONS**

---

Search radars generally require  $360^\circ$  azimuthal coverage. This coverage is difficult to obtain on an aircraft since mounting an antenna in the clear presents major drag, stability, and structural problems. When extensive vertical coverage is required, the aircraft's planform and vertical stabilizer distort and shadow the antenna pattern. Analysis of tactical requirements may show that only a limited coverage sector is required. However, this sector usually has to be capable of being positioned over the full  $360^\circ$  relative to the aircraft's heading because of the requirements for coverage while reversing course, large crab angles when high winds are encountered, need to position ground track in relation to wind, nontypical operating situations, and operational requirements for coverage while proceeding to and from the station.

## **16.3 PLATFORM MOTION AND ALTITUDE EFFECTS ON MTI PERFORMANCE**

---

MTI discriminates between airborne moving targets and stationary land or sea clutter. However, in the airborne case the clutter moves with respect to the airborne platform. It is possible to compensate for the mean clutter radial velocity

by using techniques such as TACCAR (time-averaged-clutter coherent airborne radar).

As shown in Fig. 16.2, the apparent radial velocity of the clutter is  $V_r = -V_g \cos \alpha$ , where  $V_g$  is the ground speed of the platform and  $\alpha$  is the angle subtended between the line of sight to a point on the earth's surface and the aircraft's velocity vector. Figure 16.3 shows the loci of constant radial velocity along the surface. In order to normalize the figure, a flat earth is assumed, and the normalized radial velocity  $V_n = V_r/V_g$  is presented as a function of azimuth angle  $\psi$  and normalized ground range  $R/H$ , where  $H$  is the aircraft's altitude.

Instead of a single clutter doppler frequency corresponding to a constant radial velocity ( $V_B$  in Fig. 16.2) determined by the antenna pointing angle  $\alpha_0$ , the radar sees a continuum of velocities. This results in a frequency spectrum at a particular range whose shape is determined by the antenna pattern that intersects the surface, the reflectivity of the clutter, and the velocity distribution within the beam. Furthermore, since  $V_r$  varies as a function of range at a particular azimuth  $\psi$ , the center frequency and spectrum shape vary as a function of range and azimuth angle  $\psi_0$ .

When the antenna is pointing ahead, the predominant effect is the variation of the center frequency corresponding to the change in  $\alpha_0$  with range. When the antenna is pointing abeam, the predominant effect is the velocity spread across the antenna beamwidth. These are classified as the slant-range effect and the platform-motion effect, respectively.

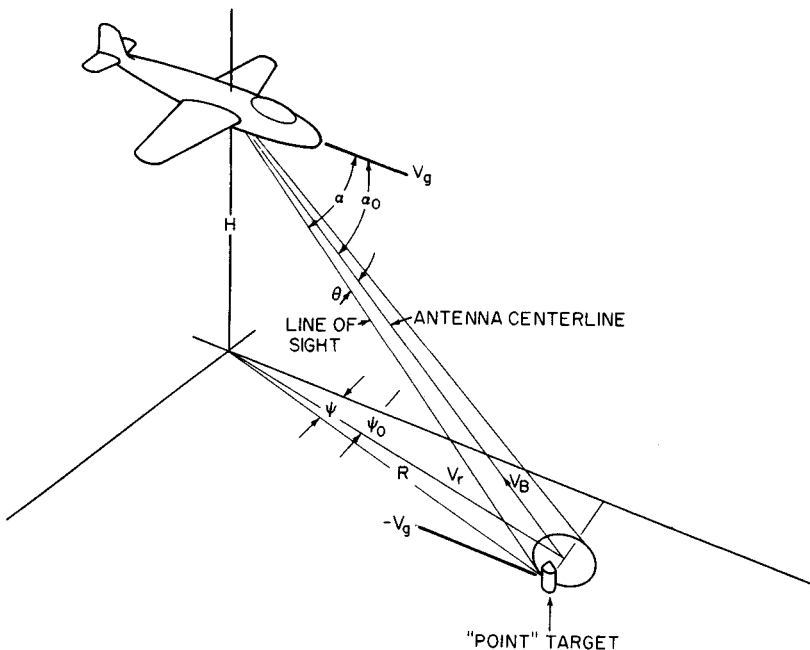


**FIG. 16.2** Defining geometry:  $\alpha_0$  = antenna pointing angle;  $\alpha$  = line-of-sight angle;  $\theta$  = angle from antenna centerline;  $V_g$  = aircraft ground speed;  $V_r$  = radial velocity of point target;  $V_B$  = radial velocity along antenna centerline (boresight);  $\psi_0$  = antenna azimuth angle;  $\psi$  = azimuth angle;  $R$  = ground range to point target;  $H$  = aircraft height.

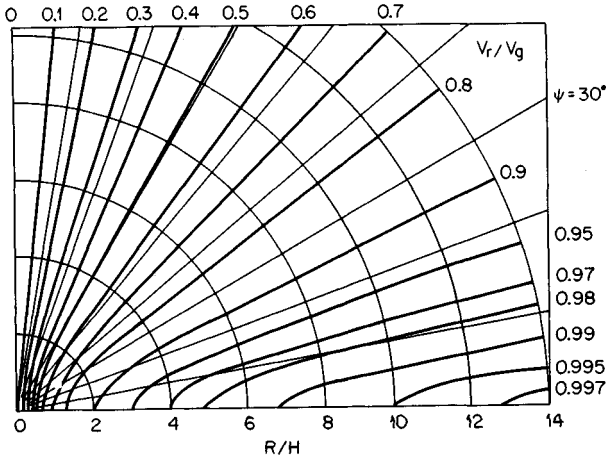


FIG. 16.3 Loci of constant normalized radial velocity  $V_r/V_g$  as a function of aircraft range-to-height ratio  $R/H$  and azimuth angle  $\psi$ .

**Effect of Slant Range on Doppler Offset.** The antenna boresight velocity  $V_B$  is the ground-velocity component along the antenna centerline (boresight) and is given as  $-V_g \cos \alpha_0$ . If the clutter surface were coplanar with the aircraft, this component would be equal to  $-V_g \cos \psi_0$  and would be independent of range. The ratio of the actual boresight velocity to the coplanar boresight velocity is defined as the normalized boresight-velocity ratio:

$$VBR = \frac{\cos \alpha_0}{\cos \psi_0} = \cos \phi_0 \tag{16.1}$$

where  $\phi_0$  is the depression angle of the antenna centerline from the horizontal. Figure 16.4 shows the variation of the normalized boresight-velocity ratio as a

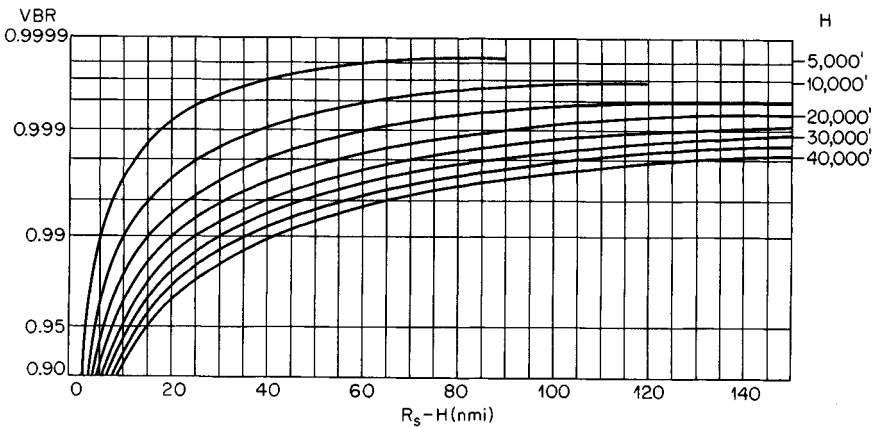


FIG. 16.4 Normalized boresight-velocity ratio  $VBR$  as a function of the difference between slant range  $R_s$  and aircraft altitude  $H$  for different aircraft altitudes.

function of slant range for a curved earth and different aircraft altitudes. The variation is fairly rapid for slant ranges less than 15 mi.

It is desirable to center the clutter spectrum in the notch (i.e., minimum-response region) of the AMTI filter in order to obtain maximum clutter rejection. This can be accomplished by offsetting the IF or RF frequency of the radar signal by an amount equal to the average doppler frequency of the clutter spectrum. Since the clutter center frequency varies with range and azimuth when the radar is moving, it is necessary for the filter notch to track the doppler-offset frequency, using an open- or closed-loop control system such as TACCAR, described below.

**TACCAR.** The MIT Lincoln Laboratory originally developed TACCAR to solve the AMTI radar problem. After many other approaches, it was recognized that if one used the clutter return rather than the transmit pulse to phase-lock the radar to the clutter filter, one could center the clutter in the filter stopband. The clutter phase varies from range cell to range cell owing to the distribution of the location of the scatterers in azimuth. Hence it is necessary to average the return for as long an interval as possible. Other processing features, such as phase comparison cancellation, were included in this radar (AN/APS-70). Today TACCAR is used to describe the centering of the returned clutter spectrum to the zero filter frequency. Since the technique compensates for drift in the various system elements and biases in the mean doppler frequency due to ocean currents, chaff, or weather clutter, it is used in shipboard and land-based radars as well as airborne radar.

A functional block diagram of an airborne radar employing TACCAR is shown in Fig. 16.5. The clutter error signal is obtained by measuring the pulse-to-pulse phase shift  $\omega_d T_p$  of the clutter return. This provides a very sensitive error signal. The averaged error signal controls a voltage-controlled coherent master oscillator (COMO), which determines the transmitted frequency of the radar. The COMO is slaved to the system reference oscillator frequency via the automatic frequency control (AFC) loop shown in Fig. 16.5. This provides a stable reference in the absence of clutter. An input from the aircraft inertial navigation system and the

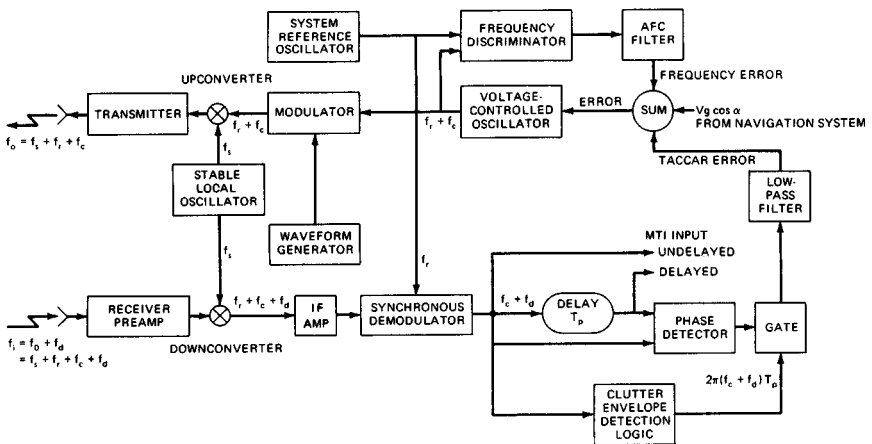


FIG. 16.5 Block diagram of a radar illustrating the signal flow path of the TACCAR control loop.

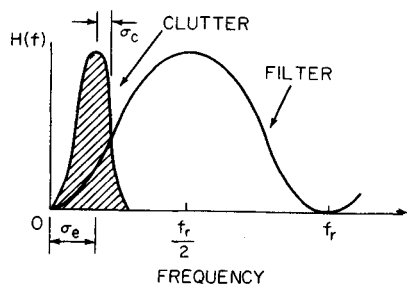


FIG. 16.6 Effect of doppler-offset error;  $f_r = \text{PRF}$ .

antenna servo provide a predicted doppler offset. These inputs allow the TACCAR system to provide a narrow-bandwidth correction signal.

Because of the noisy nature of the clutter signal, the need to have the control system bridge regions of weak clutter return, and the requirement not to respond to the doppler shift of a true target, the control system usually tracks the azimuth variation of a specific radar range interval. The maximum range of this interval is chosen so that clutter will be the dominant signal

within the interval. The minimum range is chosen to exclude signals whose average frequency differs substantially from the frequency in the region of interest. For some applications it may be necessary to use multiple control loops, each one covering a specific range interval, or to vary the offset frequency in range. At any particular range the filter notch is effectively at one frequency and the center frequency of the clutter spectrum at another. The difference between these frequencies results in a doppler-offset error as shown in Fig. 16.6. The clutter spectrum will extend into more of the filter passband, and the improvement factor will be degraded.

Figure 16.7 shows the improvement factor for single- and double-delay cancelers as a function of the ratio of the notch-offset error to the pulse repetition frequency (PRF) for different clutter spectral widths. Fortunately, the platform-motion spectrum is narrow in the forward sector of coverage where offset error is

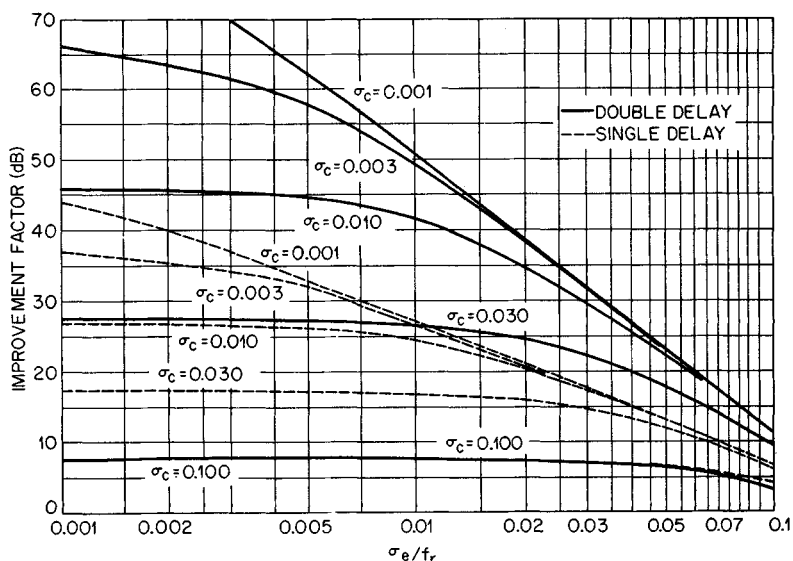


FIG. 16.7 Improvement factor  $I$  versus normalized doppler offset  $\sigma_e$  as a function of clutter spectrum width  $\sigma_c$ .

maximum. An offset error of one-hundredth of the PRF would yield 26 dB improvement for a double canceler with an input clutter spectrum whose width was 3 percent of the PRF. If the radar frequency were 10 GHz, PRF 1 kHz, and ground speed 580 kn, the notch would have to be held within 0.29 kn or  $0.005V_g$ .

Because of these requirements and the width of the platform-motion spectrum, stagger PRF systems must be chosen primarily on the basis of maintaining the stopband rather than flattening the passband. Similarly, higher-order delay-line filters (with or without feedback) are synthesized on the basis of stopband rejection. The limiting case is the narrowband filter bank where each individual filter consists of a small passband, the balance being stopband.

**Platform-Motion Effect.** To an airborne radar a clutter scatterer appears to have a radial velocity that differs from the antenna-boresight radial velocity at the same range by

$$\begin{aligned} V_e &= V_r - V_B \\ &= V_g \cos \alpha_0 - V_g \cos \alpha \\ &= V_g [\cos \alpha_0 - \cos (\alpha_0 + \theta)] \\ &= V_x \sin \theta + 2V_y \sin^2 \frac{\theta}{2} \end{aligned} \quad (16.2)$$

for small values of  $\theta$  and depression angle  $\phi_0$ , where  $V_x$  is the horizontal component of velocity perpendicular to the antenna boresight and  $V_y$  is the component along the antenna boresight.  $\theta$  is the azimuthal angle from the antenna boresight, or intersection of the vertical plane containing the boresight with the ground. The corresponding doppler frequency, when  $\alpha_0$  is a few beamwidths from ground track, is

$$f_d = \frac{2V_x}{\lambda} \sin \theta \approx \frac{2V_x}{\lambda} \theta \quad (16.3)$$

This phenomenon results in a platform-motion clutter power spectrum which is weighted by the antenna's two-way power pattern in azimuth. The true spectrum may be approximated by a gaussian spectrum,

$$H(f) = e^{-1/2(f_d/\sigma_{pm})^2} = e^{-(V_x \theta / \lambda \sigma_{pm})^2} \approx G^4(\theta) \quad (16.4)$$

$G^4(\theta)$ , the two-way power pattern of the antenna, is 0.25 when  $\theta = \theta_a/2$ , where  $\theta_a$  is the half-power beamwidth which can be approximated by  $\lambda/\alpha$ ,  $\alpha$  being the effective horizontal aperture width. Thus

$$e^{-1/2(V_x/a\sigma_{pm})^2} = 0.25$$

or

$$\sigma_{pm} = 0.6 \frac{V_x}{a} \quad (16.5)$$

where  $V_x$  and  $a$  are in consistent units. This value is lower than ones derived by other authors.<sup>4,5</sup> However, it agrees with more exact analysis of antenna radiation patterns and experimental data analyzed by the author.

A more exact value of the parameter  $\sigma_{pm}$  may be obtained by matching a two-

way power pattern of interest with the gaussian approximation at a specific point on the pattern, determining the standard deviation of  $\theta$  by using statistical techniques, or fitting the pattern and using numerical methods. The calculation of the improvement factor  $I$  can be performed by averaging the resultant residue power, obtained by summing the signal phasors at specific values of  $\theta$ , from null to null of the antenna pattern.

Figure 16.8 shows the effect of platform motion on the MTI improvement factor as a function of the fraction of the aperture displaced in the plane of the aperture per interpulse period  $T_p$ . A 5.4 percent displacement would reduce the double-delay improvement factor to 30 dB. This corresponds to a speed of 540 ft/s if the system has a PRF of 1000 Hz and a 10-ft antenna aperture. For a single-delay system the displacement would have to be held to 1.1 percent for a 30 dB performance limit.

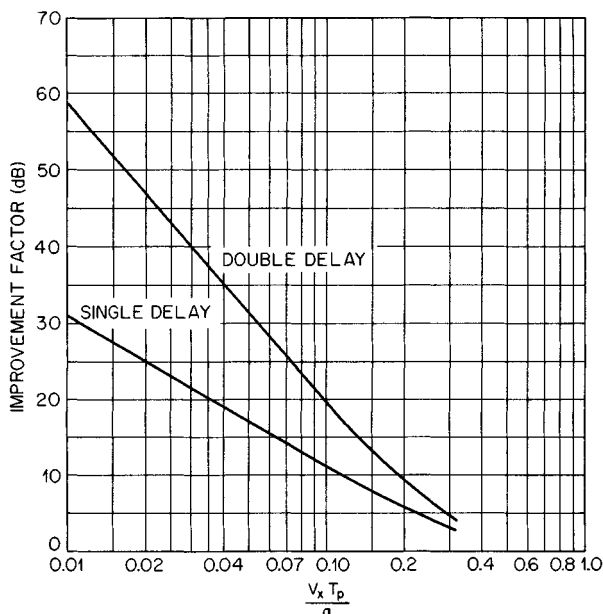
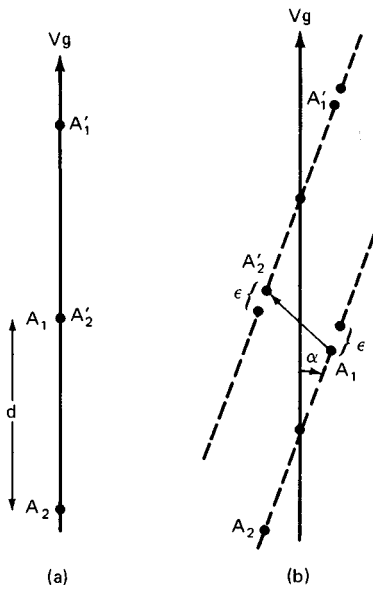


FIG. 16.8 Effect of platform motion on the MTI improvement factor as a function of the fraction of the horizontal antenna aperture displaced per interpulse period,  $V_x T_p / a$ .

## 16.4 PLATFORM-MOTION COMPENSATION ABEAM

The deleterious effects of platform motion can be reduced by physically or electronically displacing the antenna phase center along the plane of the aperture. This is referred to as the displaced phase center antenna (DPCA) technique.<sup>7-11</sup>

**Physically Displaced Phase Center Antenna.** In physical DPCA,<sup>10,11</sup> the



**FIG. 16.9** Physical DPCA defining geometry. (a) Perfect motion compensation, where  $A_1$  and  $A_2$  are the antenna phase centers for pulse 1 and the primed quantities are for pulse 2. (b) Imperfect motion compensation due to displacement error and alignment error  $\alpha$ .

though the aircraft were flying at a speed and heading such that the displacement  $A_1 - A_2$  occurs during an interpulse period. The TACCAR circuits could center the resultant spectrum at zero-doppler frequency. However, the cancellation will correspond to a value  $V_x T_p = 2\epsilon$  in Fig. 16.8. If  $2\epsilon/T_p$  is small enough, then the sidelobe clutter spectrum will be in the filter notch and will be canceled.

The two-antenna scheme is difficult to mechanize, and additional errors can occur if the antennas are mounted one above the other because of antenna field variations. These variations are caused by the difference in physical location due to vertical displacement, the effect of the different near-field environments, and fabrication errors. Furthermore, the PRF is effectively cut in half by having to receive during the unique alternate transmission-path configurations. A single-antenna scheme is possible by using an array with multiple feed structures that utilize a common set of elements and a switching network as shown in Fig. 16.10. The top row of switches connects the elements to the corporate feed or to the dummy loads. The bottom row of switches connects the corporate feed to the appropriate elements. The left six elements are active in the configuration illustrated. When the switches are placed in the alternate configuration, the right six elements are active. The subarrays are displaced from each other by two elements in the example.

Another variant is to have separate corporate feeds for the left and right subarrays of the antenna.<sup>11</sup> One of the subarrays or a central group of elements is

apertures of two side-looking antennas are aligned parallel with the aircraft longitudinal axis. Their phase centers are separated by the distance  $d$ . If the aircraft is moving at ground speed  $V_g$ , then the phase centers move  $V_g T_p$  during the interpulse period  $T_p$ .

In Fig. 16.9a the first pulse is transmitted and received on the forward antenna  $A_1$ . The second pulse is transmitted and received on the rear antenna  $A_2$  during the next interpulse period. If  $d = V_g T_p$ , then the antenna used on the first pulse,  $A_1$ , will coincide with the antenna  $A_2$  used on the second pulse. On a two-pulse-pair basis the signals received at  $A_1$  and  $A_2$  make it appear as if the antenna were stationary. There is actually a displacement with respect to the transmitter, but the signal path difference will be the same pulse to pulse. This will appear as a negligible range error.

Since it is difficult to change the spacing between antennas, the displacement is set by the design speed and PRF limits. Then the PRF is varied during operation to maintain the proper alignment.

If the antenna is not aligned with the flight path and if  $d$  is not equal to  $V_g T_p$ , then an error occurs between  $A_1$  and  $A_2$  as shown in Fig. 16.9b. The result is as

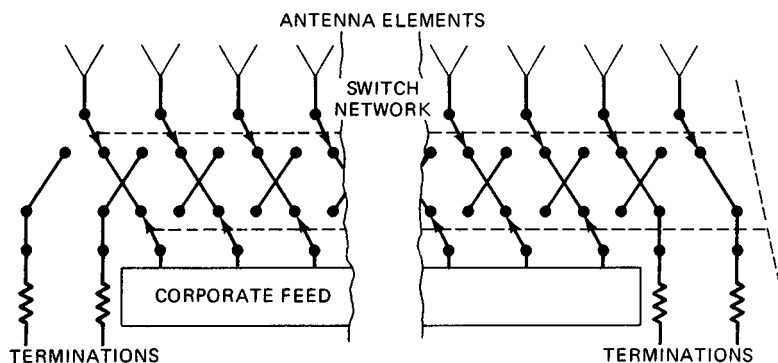


FIG. 16.10 Switching network to synthesize displaced subarrays, within an antenna array.

used as the transmit array to avoid high-power switching circuits. The separation of the subarrays  $d$  must equal  $2V_x T_p$  to compensate for the transmit phase-center displacement. This allows  $A_1 - A'_2$  to be paired and then  $A'_1$  to be paired with  $A''_2$ , where  $A_1$  is displaced from  $A_2$  by  $d$ . This allows cancellation to be made every interpulse period, maintaining the effective PRF equal to the basic PRF.

The two-way patterns from the antenna at  $A_1$  and  $A_2$  must be nearly identical; otherwise, cancellation will be degraded. This degradation may be calculated by measuring the two antenna patterns,  $G_1(\theta)$  and  $G_2(\theta)$ , and then calculating the correlation coefficient

$$\rho = \frac{[\int G_1^2(\theta)G_2^{*2}(\theta)d\theta]^2}{\int [G_1(\theta)]^4 d\theta \int [G_2(\theta)]^4 d\theta} \quad (16.6)$$

The resultant cancellation ratio is then

$$CR = 10 \log [1/(1 - \rho)] \quad (16.7)$$

If  $G_2(\theta)$  is nearly identical to  $G_1(\theta)$ , then  $\rho$  is approximately equal to 1 and the cancellation ratio is large. When measuring  $G_1$  and  $G_2$ , the array must be displaced for the second measurement to ensure that each subarray is in the same physical position on the antenna range.

**Electronically Displaced Phase Center Antenna.** Figure 16.11a shows the pulse-to-pulse phase advance of an elemental scatterer as seen by the radar receiver. The amplitude  $E_1$  of the received signal is proportional to the two-way antenna field intensity. The phase advance is

$$2\eta = 2\pi f_d T_p = \frac{4\pi V_x T_p \sin \theta}{\lambda} \quad (16.8)$$

where  $f_d$  = doppler shift of scatterer [Eq. (16.3)]  
 $T_p$  = interpulse period

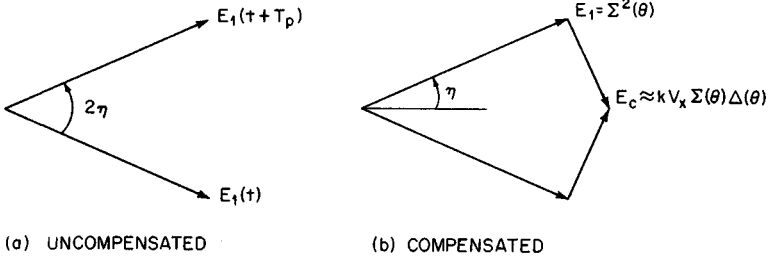


**FIG. 16.11** Phasor diagram showing the return from a point scatterer due to platform motion.

Figure 16.11*b* shows a method of correcting for the phase advance  $\eta$ . An idealized correction signal  $E_c$  is applied, leading the received signal by  $90^\circ$  and lagging the next received signal by  $90^\circ$ . For exact compensation the following relation would hold:

$$E_c = E_1 \tan \eta = \Sigma^2(\theta) \tan \frac{2\pi V_x T_p \sin \theta}{\lambda} \quad (16.9)$$

This assumes a two-lobe antenna pattern similar to that in a monopulse tracking radar. Two receivers are used, one supplying a sum signal  $\Sigma(\theta)$  and the other a difference signal  $\Delta(\theta)$ . The difference signal is used to compensate for the effects of platform motion.

If the system is designed to transmit the sum pattern  $\Sigma(\theta)$  and receive both  $\Sigma(\theta)$  and a difference pattern  $\Delta(\theta)$ , then at the design speed the received signal  $\Sigma(\theta)\Delta(\theta)$  can be applied as the correction signal. The actual correction signal used to approximate  $E_c$  is  $k \Sigma(\theta)\Delta(\theta)$ , where  $k$  is the ratio of the amplification in the sum and difference channels of the receiver.

A uniformly illuminated monopulse array<sup>12</sup> has the difference signal  $\Delta$  in quadrature with the sum and has the amplitude relationship

$$\Delta(\theta) = \Sigma(\theta) \tan \left( \frac{\pi W}{\lambda} \sin \theta \right) \quad (16.10)$$

where  $W$  is the distance between the phase centers of the two halves of the antenna. Hence a choice of  $W = 2V_x T_p$  and  $k' = 1$  would ideally result in perfect cancellation.

In practice, a sum pattern is chosen based on the desired beamwidth, gain, and sidelobes for the detection system requirements. Then the difference pattern  $\Delta(\theta)$  is synthesized independently, based on the relationship required at design radar platform speed and allowable sidelobes. The two patterns may be realized by combining the elements in separate corporate-feed structures.

Figure 16.12 shows the idealized improvement factor as a function of normalized aperture movement for a double-delay canceler. The improvement factor shown is the improvement factor for a point scatterer averaged over the null-to-null antenna beamwidth. In one case the gain ratio  $k'$  is optimized at each value of pulse-to-pulse displacement. In the other compensated case the optimum gain ratio  $k$  is approximated by the linear function of interpulse platform motion  $kV_x$ .

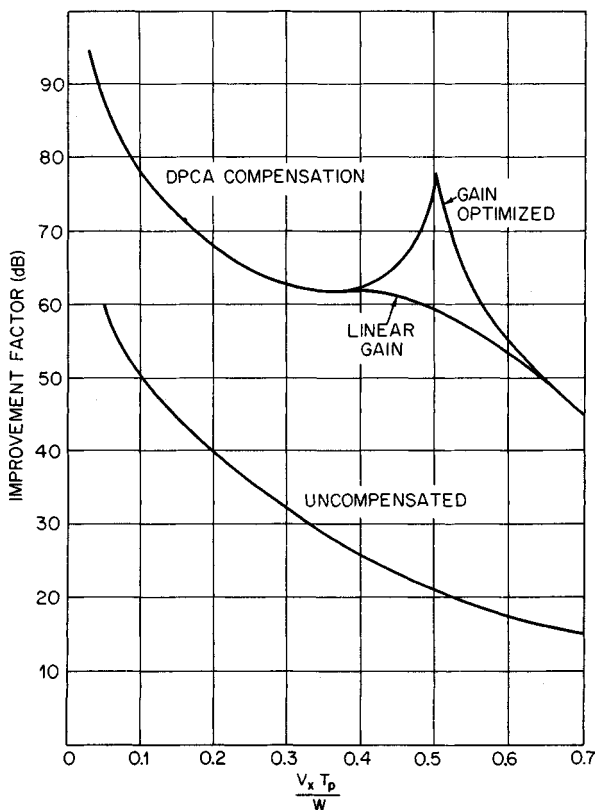


FIG. 16.12 MTI improvement factor  $I$  for DPCA compensation as a function of the fraction of the horizontal phase center separation  $W$  that the horizontal antenna aperture is displaced per interpulse period,  $V_x T_p / W$ .  $W = 0.172a$ .

A block diagram of the double-delay system is shown in Fig. 16.13. Since the transmitted pattern  $\Sigma(\theta)$  appears in both channels, it is not shown. A single-delay system would not have the second delay line and subtractor. The normally required circuitry for maintaining coherence, gain and phase balance, and timing is not shown. The speed control  $V_x$  is bipolar and must be capable of reversing the sign of the  $\Delta(\theta)$  signal in each channel when the antenna pointing angle changes from the port to the starboard side of the aircraft.

The hybrid amplifier shown has two input terminals which receive  $\Sigma(\theta)$  and  $j\Delta(\theta)$  and amplify the  $\Delta(\theta)$  channel by  $kV_x$  relative to the  $\Sigma(\theta)$  channel. The output terminals produce the sum and difference of the two amplified input signals. Since DPCA compensates for the complex signal, both amplitude and phase information must be retained. Therefore, these operations usually occur at RF or IF. Digital compensation can be used if synchronous detection and analog-to-digital (A/D) conversion are performed and the components are treated as complex phasors. Furthermore, the operations must be linear until the sum signal and difference signals have been processed by the hybrid amplifier. After this

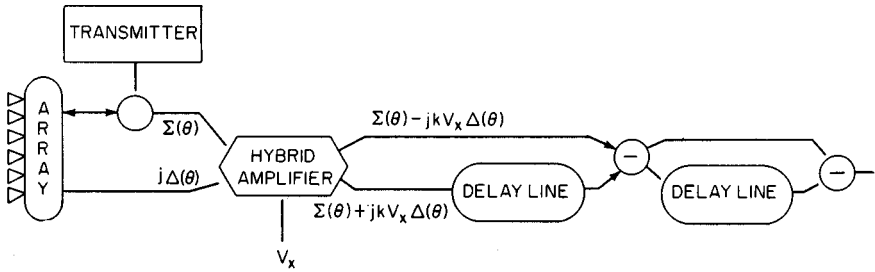


FIG. 16.13 Simplified double-delay DPCA mechanization.

single-pulse combination, the actual double cancellation can be performed by any of the processing techniques outlined in Chap. 15.

**Power in the Antenna Sidelobes.** Airborne systems are limited in their ability to reject clutter due to the power returned by the antenna sidelobes. The full  $360^\circ$  azimuthal pattern sees velocities from  $-V_g$  to  $+V_g$ . The compensation circuits offset the velocity by an amount corresponding to the antenna boresight velocity  $V_B$ , but the total range of doppler frequencies corresponding to  $2V_g$  is obtained because of echoes received via the sidelobes. For airborne systems with low and medium PRFs, these doppler frequencies can cover several multiples of the PRF so that the sidelobe power is folded into the filter. This limitation is a function of the antenna pointing angle, the MTI filter response, and the sidelobe pattern. If the sidelobes are relatively well distributed in azimuth, a measure of performance can be obtained by averaging the power returned by the sidelobes.

The limiting improvement factor due to sidelobes is

$$I_{\text{sl limit}} = \frac{K \int_{-\pi}^{\pi} G^4(\theta) d\theta}{\int_{\text{sl}} G^4(\theta) d\theta} \quad (16.11)$$

where the lower integral is taken outside the main-beam region. Main-beam effects would be included in the platform-motion improvement factor. The constant  $K$  is the noise normalization factor for the MTI filter. ( $K = 2$  for single delay and 6 for double delay.)  $G^4(\theta)$  is the two-way power of the antenna in the plane of the ground surface.

The DPCA performance described in the preceding subsection can be analyzed on the basis of radiation patterns or the equivalent aperture distribution function.<sup>8</sup> If the radiation pattern is used, the composite performance may be obtained either by applying the pattern functions over the entire  $360^\circ$  pattern or by combining the improvement factors for the DPCA main-beam and the sidelobe regions in the same manner as parallel impedances are combined:

$$\frac{1}{I_{\text{total}}} = \frac{1}{I_{\text{sl}}} + \frac{1}{I_{\text{DPCA}}} \quad (16.12)$$

If the aperture distribution is used, the sidelobe effects are inherent in the analysis. Care must be taken since if the array or reflector function is used with-

out considering the weighting of the elemental pattern or the feed distribution, the inherent sidelobe pattern can obscure the main-beam compensation results.

## 16.5 SCANNING-MOTION COMPENSATION

Figure 16.14a shows a typical antenna main-beam radiation pattern and the response of a point scatterer for two successive pulses when the antenna is scanning. It is seen that the signals returned would differ by  $\Delta G^2(\theta)$ . This results in imperfect cancellation due to scanning. The average effect on the improvement factor can be obtained by integrating this differential effect over the main beams:

$$I_{\text{scan}} = \frac{2 \int_{-\theta_0}^{\theta_0} |G(\theta)|^2 d\theta}{\int_{-\theta_0}^{\theta_0} |G(\theta + T_p \dot{\theta}) - G(\theta)|^2 d\theta} \quad \text{for single-delay cancellation} \quad (16.13a)$$

$$I_{\text{scan}} = \frac{6 \int_{-\theta_0}^{\theta_0} |G(\theta)|^2 d\theta}{\int_{-\theta_0}^{\theta_0} |G(\theta + T_p \dot{\theta}) - 2G(\theta) + G(\theta - T_p \dot{\theta})|^2 d\theta} \quad \text{for double-delay cancellation} \quad (16.13b)$$

where  $\theta_0$  = null of main beam

$G(\theta)$  = two-way voltage pattern

In order to treat scanning motion in the frequency domain, the apparent clutter velocity seen by the scanning antenna is examined to determine the doppler frequency. Each element of an array or incremental section of a continuous aperture can be considered as receiving a doppler-shifted signal due to the relative

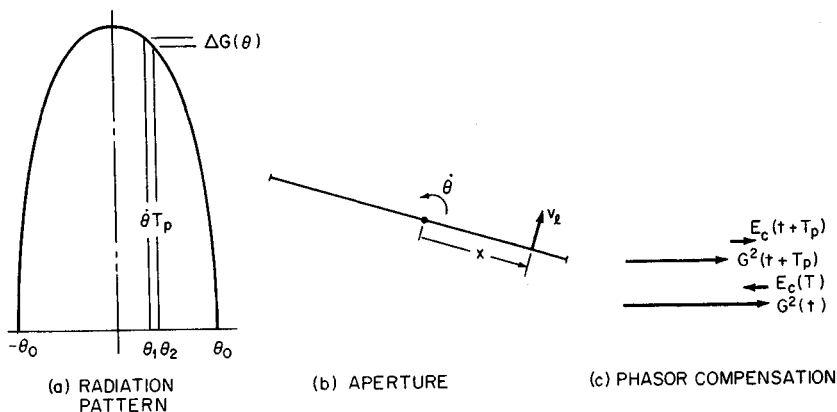


**FIG. 16.14** Antenna scanning effects. (a) As seen by the antenna radiation pattern, due to the apparent change in azimuth of the scatterer,  $\theta_2 - \theta_1 = \dot{\theta} T_p$ . (b) As seen by the aperture illumination function, due to the apparent motion,  $v_x = x \dot{\theta}$ , of the scatterer relative to the antenna element at position  $x$ . (c) Step-scan compensation of two received phasors.

motion of the clutter. The power received by the element is proportional to the two-way aperture power distribution function  $F_2(x)$  at the element.

In addition to the velocity seen by all elements because of the motion of the platform, each element sees an apparent clutter velocity due to its rotational motion, as illustrated in Fig. 16.14b. The apparent velocity varies linearly along the aperture. Hence the two-way aperture distribution is mapped into the frequency domain. The resulting power spectrum due to the antenna scanning is

$$H(f) \approx F_2\left(\frac{\lambda f}{2\dot{\theta}}\right) \quad 0 \leq f \leq \frac{a\dot{\theta}}{\lambda} \quad (16.14)$$

where  $\dot{\theta}$  = antenna rotation rate  
 $a$  = horizontal antenna aperture

This spectrum can be approximated by a gaussian distribution with standard deviation

$$\sigma_c = 0.265 \frac{f_r}{n} = 0.265 \frac{\dot{\theta}}{\theta_a} \approx 0.265 \frac{a\dot{\theta}}{\lambda} \quad (16.15)$$

where  $\lambda$  and  $a$  are in the same units,  $\theta_a$  is the one-way half-power beamwidth, and  $n$  is the number of hits per beamwidth. The approximation  $\theta_a \approx \lambda/a$  is representative of antenna distribution yielding acceptable sidelobe levels.

It can be seen that the differential return is

$$\Delta G^2(\theta) \approx \frac{dG^2(\theta)}{d\theta} \Delta\theta = \frac{dG^2(\theta)}{d\theta} \dot{\theta} T_p \quad (16.16)$$

This suggests<sup>7,13</sup> that a correction signal in the reverse sense to  $\Delta G^2(\theta)$  be applied, as shown in Fig. 16.14c. Half the correction is added to one pulse and half subtracted from the other, so that

$$\begin{aligned} \text{Correction signal} &= \frac{\Delta G^2(\theta)}{2} = \frac{\dot{\theta} T_p}{2} \frac{d\Sigma^2(\theta)}{d\theta} \\ &= \dot{\theta} T_p \Sigma(\theta) \frac{d\Sigma(\theta)}{d\theta} \end{aligned} \quad (16.17)$$

where  $\Sigma^2(\theta)$  was substituted for  $G^2(\theta)$ . The radar transmits a sum pattern  $\Sigma(\theta)$  and receives on the difference pattern  $\Delta(\theta)$ , so that the received signal is proportional to the product of the two. If the signal received on the difference pattern is used as the correction, we have

$$E_c = \Delta(\theta)\Sigma(\theta) \quad (16.18)$$

By comparing Eqs. (16.17) and (16.18), we see that, for  $E_c$  to approximate the correction signal, the difference patterns should be

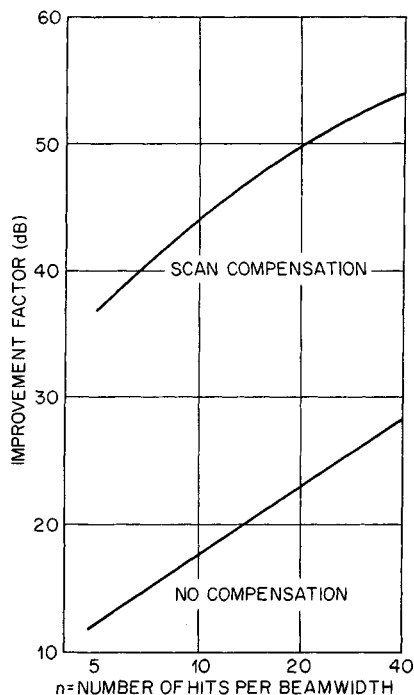


FIG. 16.15 MTI improvement factor for a step-scan compensation of a single-delay canceler as a function of the number of hits per beamwidth. The antenna pattern is  $(\sin x)/x$ .

Figure 16.15 shows the improvement obtained by Dickey and Santa<sup>7</sup> for single-delay cancellation.

**Compensation-Pattern Selection.** Selection of the compensation pattern depends on the level of system performance required, the type of MTI filtering used, the platform velocity, scan rate, and the characteristics required by normal radar parameters such as resolution, distortion, gain, sidelobes, etc. For instance, an exponential pattern and its corresponding difference pattern are excellent for single-delay-cancellation DPCA but are unsatisfactory when double-delay cancellation is used. This is because the single-delay canceler requires the best match between the actual pattern and the required pattern near boresight, whereas double cancellation requires the best match on the beam shoulder. Step-scan compensation usually requires the difference-pattern peaks to be near the nulls of the sum pattern to match.

Grissetti et al.<sup>13</sup> have shown that for step-scan compensation the improvement factor for single-delay cancellation increases as a function of the number of hits at

$$\Delta(\theta) = \dot{\theta} T_p \frac{d\Sigma(\theta)}{d\theta} \quad (16.19)$$

The derivative of the sum pattern is similar to a difference pattern in that it is positive at the main-beam null,  $-\theta_0$ , and decreases to zero on the antenna centerline and then goes negative until  $\theta_0$ .

By referring to Fig. 16.13, one observes that the mechanization for scan compensation is fundamentally similar to the DPCA mechanization except that the difference signal is applied in phase with the sum signal and amplified by an amount determined by the antenna rotation per interpulse period.

The signals required, if the transmission signal  $\Sigma(\theta)$  that appears in each channel is neglected, are  $\Sigma(\theta) \pm \dot{\theta} T_p \Delta(\theta)$ , where  $\Gamma$  is the ratio of the amplification in the two channels chosen to maximize the clutter rejection. The required difference-pattern slope is determined by the derivative of the scan pattern, which differs from the DPCA criterion. This technique is known as step-scan compensation because the system electronically points the antenna slightly ahead of and behind boresight each pulse so that a leading and lagging pair are taken from successive returns to obtain the effect of the antenna remaining stationary.

20 dB/decade; for the first-derivative\*-type step-scan compensation, at the rate of 40 dB/decade; and with first- and second-derivative compensation, at the rate of 60 dB/decade. Hence, for a ground-based system that is limited by scan rate, one should improve the compensation pattern rather than use a higher-order MTI canceler. However, airborne systems are primarily limited by platform motion and require both better cancelers and compensation for operation in a land clutter environment. In the sea clutter environment the system is usually dominated by the spectral width of the velocity spectrum or platform motion rather than scanning. The applicability of DPCA or step-scan compensation in the latter case is dependent on the particular system parameters.

## 16.6 SIMULTANEOUS PLATFORM MOTION AND SCAN COMPENSATION

In AMTI systems having many hits per scan, scanning is a secondary limitation for an uncompensated double canceler. However, the performance of a DPCA system is significantly reduced when it is scanned. This is due to the scanning modulation on the difference pattern used for platform-motion compensation.

Since the DPCA applies the difference pattern in quadrature to the sum pattern to compensate for phase error and step scan applies the difference pattern in phase to compensate for amplitude error, it is possible to combine the two techniques by properly scaling and applying the difference pattern both in phase and in quadrature. The scaling factors are chosen to maximize the improvement factor under conditions of scanning and platform motion.

The relationships for a double-delay (three-pulse) AMTI are shown in the phasor diagram, Fig. 16.16. The phase advance between the first pair of pulses, received by the sum pattern  $\Sigma$ , is

$$2_{\eta_1} = \frac{4\pi T_p}{\lambda} \left[ V_x \left( \sin \theta_2 - \sin \frac{\omega_r T_p}{2} \right) + V_y \left( \cos \frac{\omega_r T_p}{2} - \cos \theta_2 \right) \right] \quad (16.20)$$

and the phase advance between the second pair of pulses is

$$2_{\eta_2} = \frac{4\pi T_p}{\lambda} \left[ V_x \left( \sin \theta_2 + \sin \frac{\omega_r T_p}{2} \right) + V_y \left( \cos \frac{\omega_r T_p}{2} - \cos \theta_2 \right) \right] \quad (16.21)$$

where  $\theta_2$  is the direction of the clutter cell with respect to the antenna pointing angle when the second pulse is received and  $\omega_r$  is the antenna scan rate. The subscripts on the received signals  $\Sigma_i$  and  $\Delta_i$  indicate the pulse reception sequence.

The difference pattern  $\Delta$  is used to generate an in-phase correction for scanning motion and a quadrature correction for platform motion. This process yields the set of resultant signals  $R_{ij}$ , where the subscript  $i$  denotes the pulse pair

\*The compensation required by  $\Delta G^2(\theta)/2$  can be determined from a Taylor's series expansion of  $G^2(\theta)$ . In the preceding discussion we used the first derivative. Using higher-order terms gives an improved correction signal.

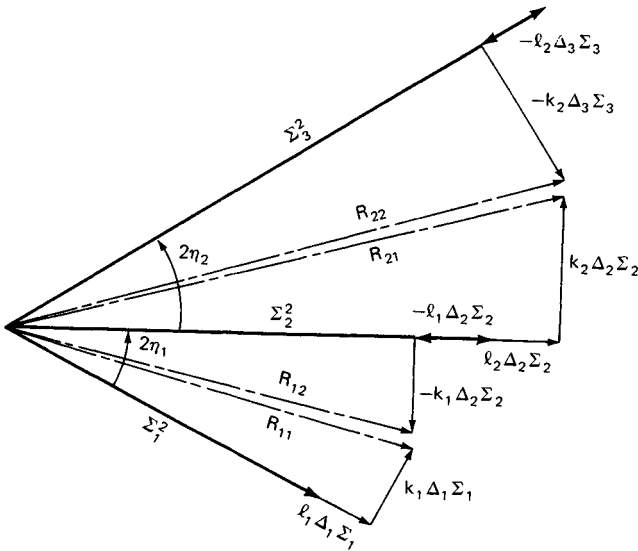


FIG. 16.16 Phasor diagram for simultaneous scanning and motion compensation.

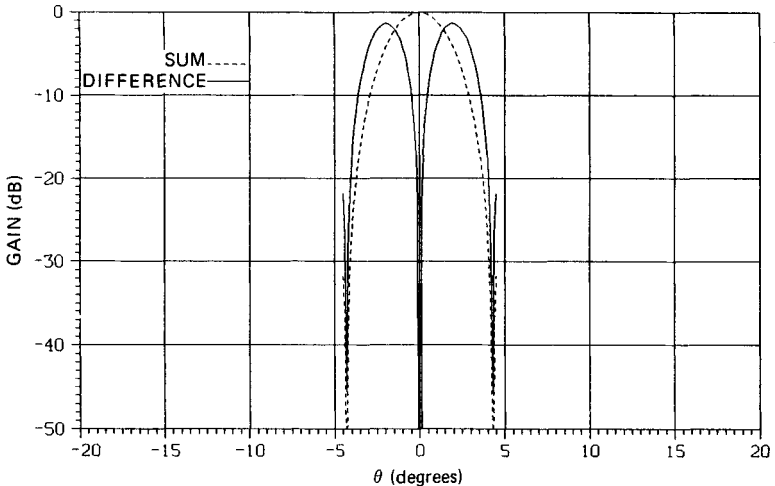


FIG. 16.17 Sum and difference patterns used to determine DPCA performance.

and the subscript  $j$  denotes the component of the pair. Since  $\eta_1$  does not equal  $\eta_2$ , different weighting constants are required for each pulse pair. The values of  $k_1$  for the quadrature correction of the first pulse pair,  $k_2$  for the quadrature correction for the second pulse pair,  $l_1$  for the in-phase correction for the first pulse pair, and  $l_2$  for the in-phase correction for the second pulse pair are optimized by minimizing the integrated residue power over the significant portion of the antenna pattern, usually chosen between the first nulls of the main beam.

Figure 16.17 shows the sum and difference main-beam patterns for an aperture

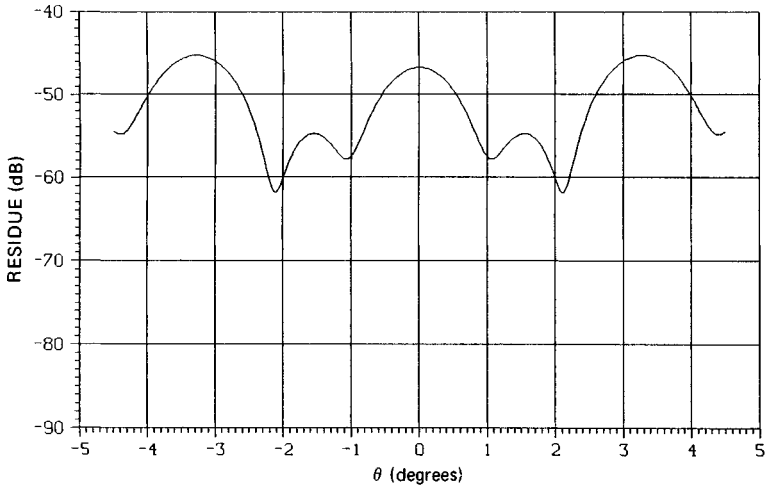


FIG. 16.18 DPCA clutter residue versus angle for normalized displacement  $V_n = 0.04$  and normalized scanning motion  $W_n = 0.04$ .

20 wavelengths long. Figure 16.18 shows the residue for the case when the fraction of the horizontal aperture width  $a$  traveled per interpulse period  $T_p$ ,  $V_n = V_x T_p / a$ , is equal to 0.04 and when the number of wavelengths that the aperture tip rotates per interpulse period,  $W_n = a \omega_r T_p / 2\lambda$ , is equal to 0.04. The corresponding improvement factor is 52 dB.

The improvement factor is shown in Fig. 16.19 for a range of normalized platform motion  $V_n$  as a function of normalized scanning displacements  $W_n$ . The

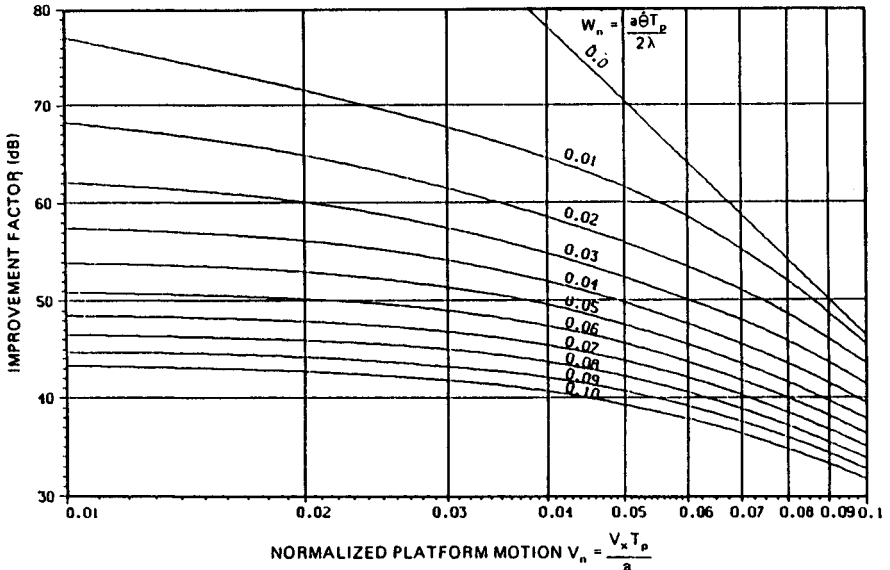


FIG. 16.19 DPCA improvement factor versus normalized platform motion  $V_n$  as a function of normalized scanning motion  $W_n$ .

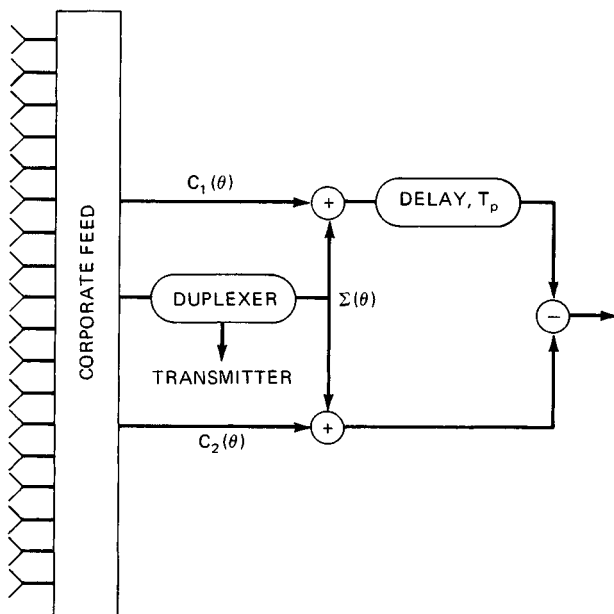


FIG. 16.20 Optimized DPCA phase compensation.

nonscanning case is shown as  $W_n = 0$ . The improvement factors were computed for the 20-wavelength aperture patterns shown in Fig. 16.17.

Andrews<sup>14</sup> has developed an optimization procedure for platform-motion compensation that rotates the phasors directly rather than by using a quadrature correction. The procedure determines the antenna feed coefficients for two compensation patterns, one of which,  $C_1(\theta)$ , is added to the sum pattern  $\Sigma(\theta)$  and fed to the undelayed canceler path and the other,  $C_2(\theta)$ , is added to the sum pattern and fed to the delayed path as shown in Fig. 16.20. The procedure was developed for a single-delay canceler and a nonscanning antenna. Andrews used the procedure to minimize the residue power over the full antenna pattern, which includes the main-beam and sidelobe regions.

## 16.7 PLATFORM-MOTION COMPENSATION, FORWARD DIRECTION

The previous sections discussed the compensation for the component of platform motion parallel to the antenna aperture. TACCAR removes the average component of platform motion perpendicular to the aperture. Wheeler Laboratories (now Hazeltine Corporation) developed the Coincident Phase Center Technique (CPCT)<sup>15</sup> to remove the spectral spread due to the velocity component perpendicular to the aperture and due to the component parallel to the aperture. Removal of the component parallel to the aperture uses the DPCA pattern synthesis technique described in Ref. 8, which creates two similarly shaped illumination

functions whose phase centers are physically displaced. Removal of the component perpendicular to the aperture is accomplished by a novel extension of this concept.

The first term of Eq. (16.2) for spectral width due to platform motion approaches zero as the antenna points ahead. However the second term of Eq. (16.2) dominates as the antenna approaches within a few beamwidths of the aircraft's ground track. In this region

$$f_d \approx \frac{4V_y}{\lambda} \sin 2 \frac{\theta}{2} \approx \frac{V_y \theta^2}{\lambda} \quad (16.22)$$

which yields a single-sided spectrum that is significantly narrower than the spectrum abeam. For moderate platform speeds and lower-frequency (UHF) radars this effect is negligible, and compensation is not required.

When it is necessary to compensate for this effect, the phase center of the antenna must be displaced ahead of the aperture and behind the aperture for alternate receive pulses so that the phase centers are coincident for a moving plat-

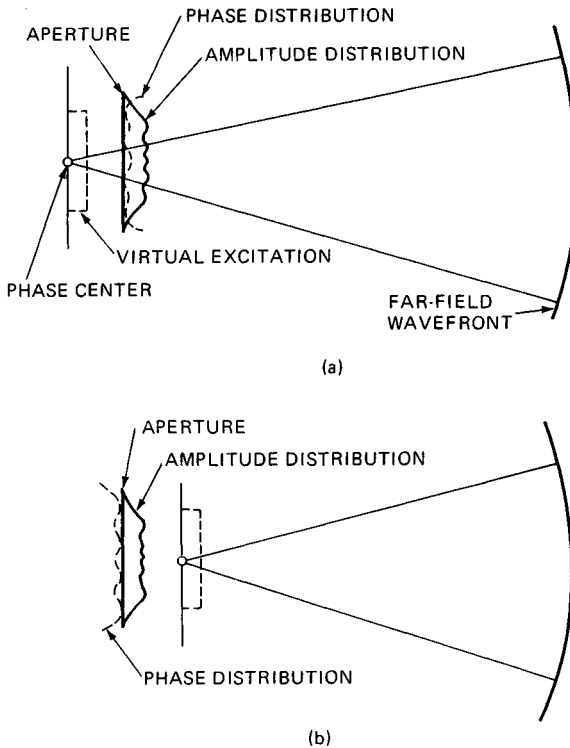


FIG. 16.21 CPCT concept showing displacement of the phase center (a) behind the physical aperture and (b) ahead of the physical aperture. (Courtesy of Hazeltine Inc.<sup>15</sup>)

form. This technique can be extended to more than two pulses by using the necessary phase-center displacements for each pulse. In order to maintain the effective PRF, the displacement must compensate for the two-way transmission path. To accomplish this displacement, near-field antenna principles are utilized. A desired aperture distribution function is specified. The near-field amplitude and phase are calculated at a given distance from the origin. If this field is used as the actual illumination function, a virtual aperture is created with the desired distribution function at the same distance behind the physical antenna. Figure 16.21a<sup>15</sup> shows the phase and amplitude distribution required to form a uniform virtual distribution displaced behind the physical aperture. It can be shown that if the phase of the illumination function is reversed  $\phi' = -\phi$ , the desired virtual distribution function is displaced ahead of the aperture as shown in Fig. 16.21b.

In practice, performance is limited by the ability to produce the required illumination function. As the displacement increases, a larger physical aperture size is required to produce the desired virtual aperture size owing to beam spreading. This can be seen in Fig. 16.21. The effectiveness of the correction varies with elevation angle since the actual displacement along the line of sight varies with elevation angle. This effect is more pronounced at higher aircraft speeds and higher radar frequencies. A change in the magnitude of the correction factor or even the compensation pattern with range, height, and velocity could be utilized to retain performance.

Figure 16.22 illustrates the theoretical MTI performance of a CPCT system as a function of beam-pointing direction and interpulse motion normalized to the interpulse motion used to design the compensation patterns. (*Cancellation ratio*

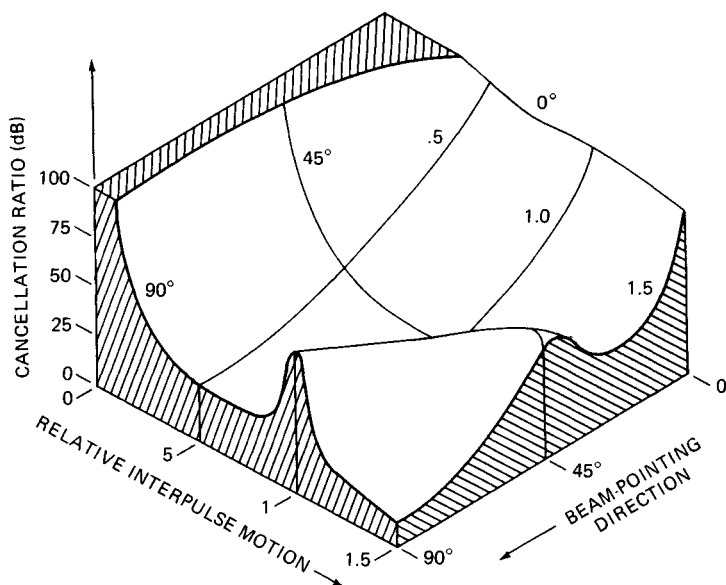


FIG. 16.22 CPCT cancellation ratio, in decibels, as a function of relative interpulse motion and beam-pointing direction. (Courtesy of Hazeltine Inc.<sup>15</sup>)

is defined as the ratio of input clutter power to output clutter residue power.) The peak on the  $90^\circ$  axis is typical of the optimized DPCA performance illustrated in Figure 16.12.

## 16.8 SPACE-TIME ADAPTIVE MOTION COMPENSATION

---

Several methods have been described to compensate for antenna motion. All these techniques are applied in the radar design phase for a specific set of operational parameters. Controls (usually automatic) are provided to adjust weights for operational conditions around the design value.

The development of digital radar technology and economical high-speed processors allows the use of dynamic space-time adaptive array processing,<sup>16</sup> whereby a set of antenna patterns that displace the phase center of the array both along and orthogonal to the array are continually synthesized to maximize the signal-to-clutter ratio. Spatial adaptive array processing combines an array of signals received at the same instant of time that are sampled at the different spatial locations corresponding to the antenna elements. Temporal adaptive array processing combines an array of signals received at the same spatial location (e.g., the output of a reflector antenna) that are sampled at different instances of time, such as several interpulse periods for an adaptive MTI. Space-time adaptive array processing combines a two-dimensional array of signals sampled at different instances of time and at different spatial locations.

A basic block diagram of a radar incorporating space-time adaptive array processing is shown in Fig. 16.23. Circuits for auxiliary functions such as pulse compression, clutter gating, synchronization, and TACCAR are not shown. With the exception of the interchange of the corporate-feed and duplexing functions, the transmit channel is identical to that of any other radar. An individual duplexer is placed between each corporate-feed output and its corresponding antenna element. Provision could be included for electronic beam steering using high-power phase shifters or transmit modules with low-power beam steering.

On receive, each duplexer output is sent to its own digital receiver and adaptive processing module (APM), which provides a weighted undelayed signal that is combined with the outputs of the other adaptive processing modules to form an undelayed antenna beam. The weighted signal received on the previous pulse is combined with the corresponding outputs of the adaptive processing modules to form a delayed antenna beam. The two beams are then subtracted to produce the single-delay AMTI output. The output is then sent to the automatic detector for further processing and display. The output is also returned to the adaptive processing modules.

Figure 16.24 shows the block diagram of a typical digital receiver. The signal received from a single antenna element is amplified and converted to IF. The IF signal is further amplified and converted to baseband by using the synchronous demodulators. One of the bipolar video outputs,  $I$ , is the component that is in phase with the reference oscillator. The other bipolar video output,  $Q$ , is in quadrature with the reference oscillator. The two bipolar video signals are sampled for each range cell and converted to digital representation by the A/D converters. The output logic formats the  $I$  and  $Q$  values for transfer to the adaptive processing module. The  $I$ ,  $Q$  pair of numbers is a phasor representing the instantaneous phase and amplitude of each range cell in rectangular coordinates.

Figure 16.25 shows a block diagram of the adaptive processing module used

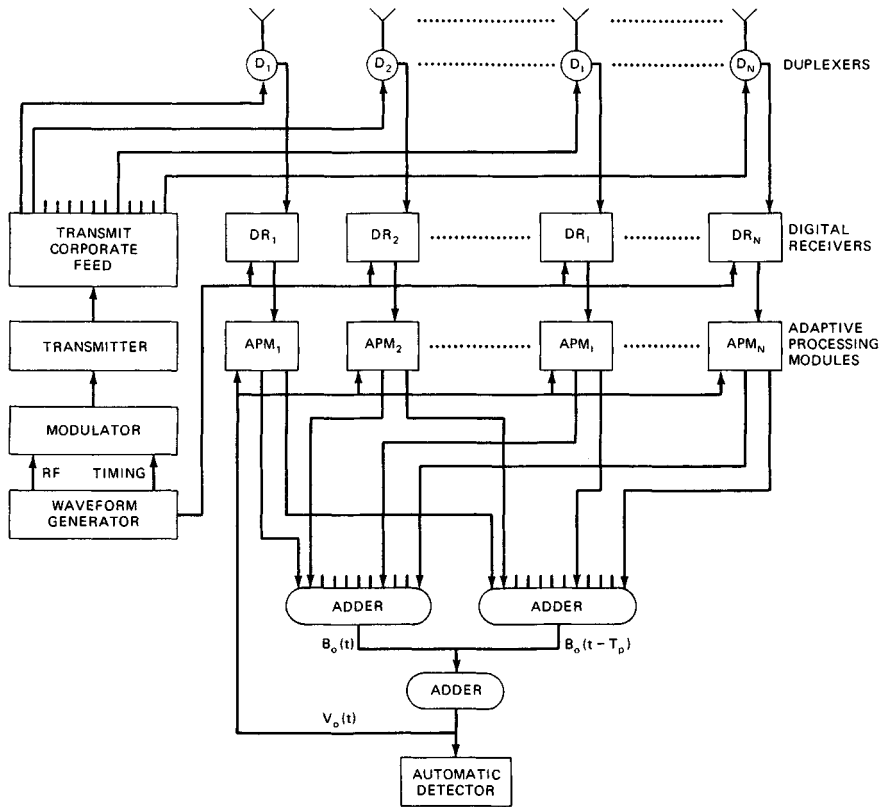


FIG. 16.23 Block diagram of a digital space-time adaptive array radar.

for space-time adaptive array processing. All components are digital processing blocks that can be implemented in various combinations of hardware and software. The complex value of the sampled signal  $V_i(t)$  is multiplied by the complex adaptive weight  $W_{i1}$  to form the  $i$ th-channel input to the adder forming the undelayed antenna beam. The value is also routed to a buffer for storage. The previously stored value  $V_i(t - T_p)$  is multiplied by the delayed channel weight  $W_{i2}$  to form the  $i$ th-channel input to the adder forming the delayed beam.

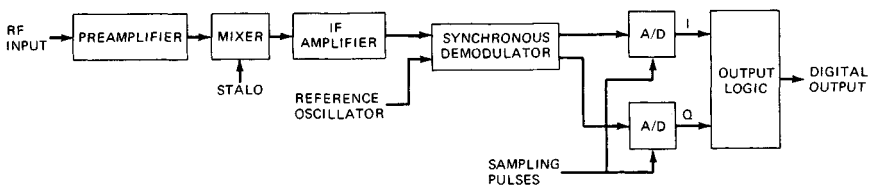


FIG. 16.24 Block diagram of a digital receiver.

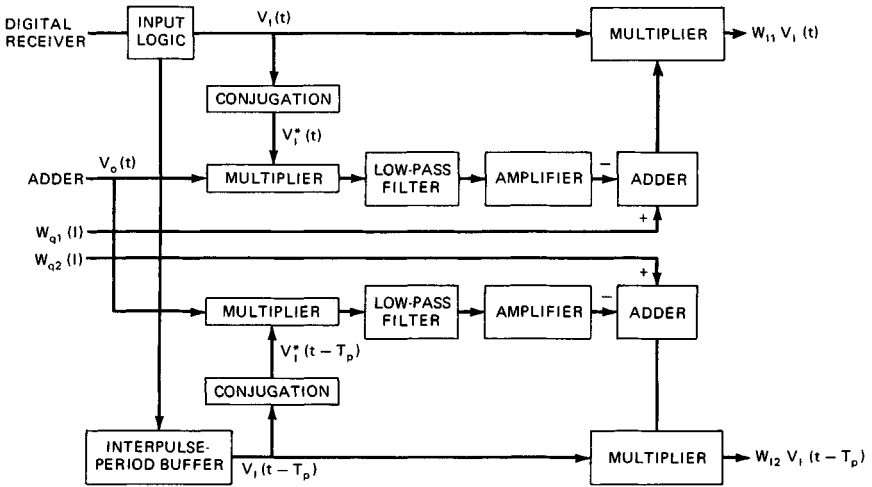


FIG. 16.25 Block diagram of an adaptive processing module.

The weights  $W_{i1}$  and  $W_{i2}$  are determined by the Howells-Applebaum algorithm.<sup>17</sup> The correlation between the input signal  $V_i(t)$  and the output signal  $V_o(t)$  is determined by multiplying  $V_o(t)$  by the complex conjugate of the input signal  $V_i^*(t)$  and averaging the resultant by passing it through a low-pass digital filter. This correlation is amplified and subtracted from the appropriate quiescent weight  $W_{q1i}$  or  $W_{q2i}$  to obtain the slowly varying weight  $W_{i1}$  or  $W_{i2}$ . The quiescent weight is the product of the antenna illumination factor for the  $i$ th element that will yield the desired antenna pattern and the MTI weight for the delayed or undelayed pulse. This would include the phase component required to steer the beam in a given direction. The closed-loop action will drive the weight so that the average correlation of the output  $V_o$  and each input  $V_i$  approximates the value of the quiescent weight.

$$\begin{aligned}
 (V_i^* V_o) &\approx W_{q1} & \text{for } i = 1 \text{ to } 2N \\
 (V_i^* \Sigma W_j V_j) &\approx W_{q1} \\
 \Sigma (V_i^* V_j) W_j &\approx W_{q1}
 \end{aligned}
 \tag{16.23}$$

where  $(\quad)$  indicates the time average. If we define the  $N$  values of each delayed variable by extending the subscript range over  $N + 1$  to  $K$ , where  $K = 2N$ , and define  $m_{ij} = (V_i^* V_j)$ , we have the set of equations

$$\begin{aligned}
 m_{11}W_1 + W_{12}W_2 + \cdots + m_{1K}W_K &= W_{q1} \\
 M_{21}W_1 + m_{22}W_2 + \cdots + m_{2K}W_K &= W_{q2} \\
 \cdot &\cdot & \cdot & \cdot & \cdot \\
 \cdot &\cdot & \cdot & \cdot & \cdot \\
 \cdot &\cdot & \cdot & \cdot & \cdot
 \end{aligned}$$

$$m_{K1}W_1 + m_{K2}W_2 + \cdots + m_{KK}W_K = W_{qK}$$

which can be expressed in matrix notation as

$$MW = W_q \quad (16.24)$$

This set of equations can be solved for the steady-state set of weights  $W_1$  to  $W_K$ , which can be expressed in matrix notation as the familiar equation

$$W = M^{-1}W_q \quad (16.25)$$

These weights have been shown<sup>17,18</sup> to be the optimum set which maximizes the signal-to-interference ratio. Because of the smoothing required to keep the weights from jittering,<sup>18</sup> the weights adapt to their steady-state values in a time determined by the clutter power and the allowable steady-state variation in the weights. Other algorithms<sup>19</sup> can speed up the adaptation rate, but a more complex mechanization is required.

This process results in a delayed beam and an undelayed beam, whose phase centers are offset to compensate for platform motion. If jamming is present in the sidelobes or on the shoulder of the main beam, nulls will be formed in each jamming direction. If mixed clutter and jamming are present, the weights will adjust to maximize the signal-to-total-interference ratio. The signal is defined as a short-duration pulse return from the direction determined by the quiescent weights and at a doppler frequency corresponding to half of the PRF. Independent quiescent weights for each subchannel could be utilized to optimize the doppler response for another frequency.

**Performance Capability of Space-Time Adaptive Arrays.** The performance attainable from the space-time array is limited by the aircraft speed, the array alignment with respect to the aircraft ground track, and the system accuracies. A performance analysis for a 16-element, two-pulse space-time array is presented in Figs. 16.26 and 16.27. The antenna elements were spaced at a half wavelength and assumed to be omnidirectional. The clutter model was assumed to be homogeneous. The improvement factor is based on the fully adapted weights. The clutter-to-noise ratio was selected to limit performance to 92 dB.

The improvement factor for adaptive arrays is usually defined as the ratio of the signal-to-interference-power ratio at the output of the processor to the signal-to-interference ratio at the input of the processor. The signal is specified as coming from the direction and at the doppler frequency specified by the quiescent weights. In MTI systems, it is customary to define the improvement factor as the average response over the doppler interval. For a single-delay processor, the MTI improvement factor is 3 dB less than the adapted improvement factor shown in Figs. 16.28 and 16.27.

Figure 16.28 shows the improvement factor for an array pointing along the ground track of the aircraft as a function of motion expressed in terms of wavelengths per interpulse period. The dashed line shows the unadapted single-delay improvement factor for an antenna with a Dolph-Chebyshev aperture illumination that provides a 28 dB uniform peak sidelobe level. The solid line shows the adapted improvement factor to be 92 dB for a stationary antenna, reducing to 89 dB for 4 wavelengths per interpulse-period platform motion. Figure 16.27 shows

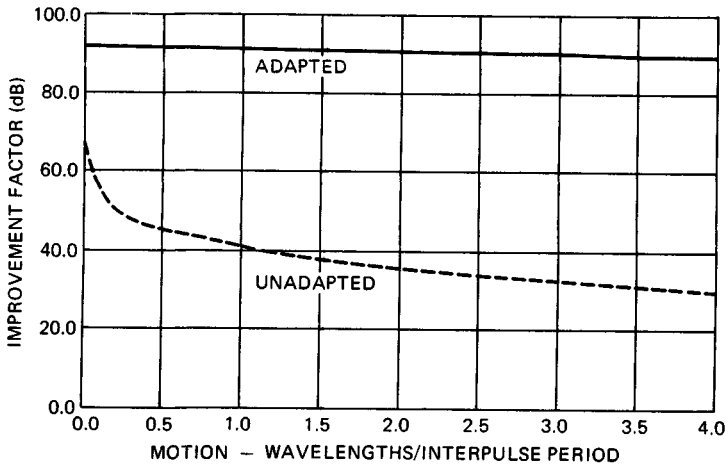


**FIG. 16.26** Adapted and unadapted improvement factor as a function of normalized antenna motion per interpulse period; 16-element (half-wavelength spacing), two-pulse space-time adaptive processor; antenna array aligned to the ground track.

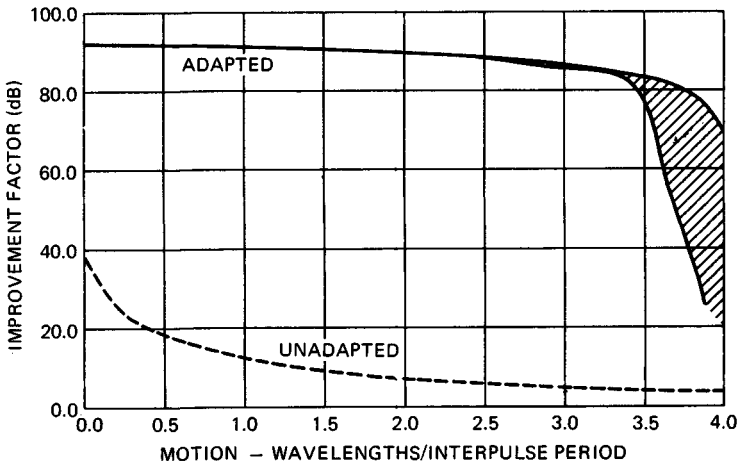


**FIG. 16.27** Adapted and unadapted improvement factor as a function of normalized antenna motion per interpulse period; 16-element (half-wavelength spacing), two-pulse space-time adaptive processor; antenna array aligned to perpendicular to the ground track.

the performance when the antenna is pointing abeam. This is the standard DPCA case. The performance holds to 1.5 wavelengths per interpulse-period platform motion, then decreases slightly, and drops off sharply above 3.5 wavelengths per interpulse period. The shaded region is where the improvement factor varies within the limits. A peak occurs when the platform motion is a multiple of a quarter wavelength. The clutter-to-noise-ratio limitation results in cusping not being

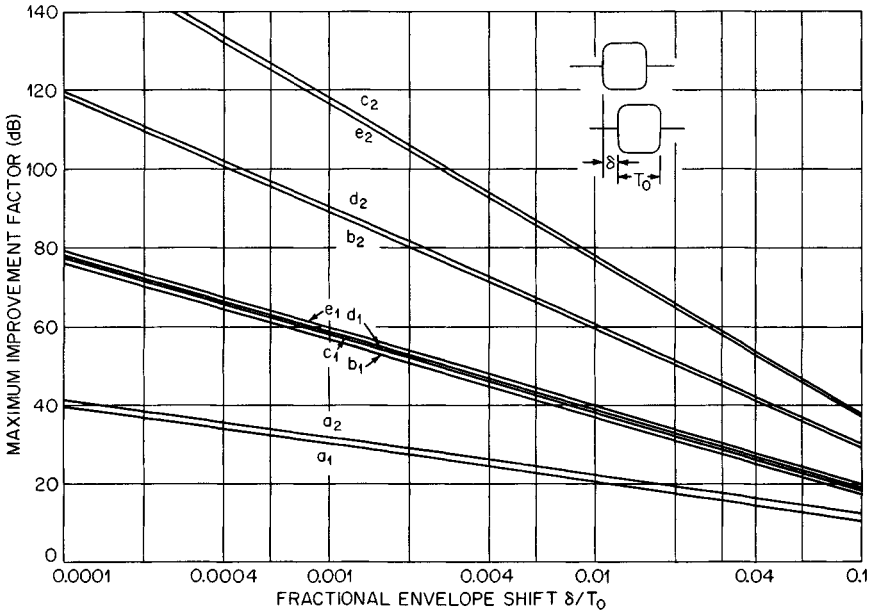


**FIG. 16.28** Maximum improvement factor as a function of a fractional envelope shift for typical pulse envelope shapes. Subscript 1 indicates single delay; 2, double delay. Pulse shape  $a$  = rectangular;  $b$  = cosine;  $c$  = cosine-squared;  $d$  = triangular;  $e$  = gaussian.

visible at speeds less the 3.5 wavelengths per interpulse period. The performance at other angles is between these two cases, and peaking does not occur.

**16.9 LIMITATION OF IMPROVEMENT FACTOR DUE TO PULSE ENVELOPE SHIFT**

The doppler frequency that arises because of the radial component of aircraft motion results in an incremental phase shift between successive radar pulses.

The envelope of the radar pulse is also delayed a corresponding amount. The TACCAR circuit usually compensates for the phase delay at IF by changing the phase of a CW reference oscillator. Hence the envelope of a single pulse is unaffected. The mismatch in the envelope delay time between successive pulses results in a residual signal, sometimes called *ranging noise*.

Figure 16.28 shows the effect of this residual on the performance of a single-delay canceler. The idealized rectangular pulse envelope gives a pessimistic picture of this effect. Most conventional representations of pulse shape give about the same performance, 20 dB per decade.

Figure 16.28 also shows the effect of the residual on a double cancellation system. In the case of double-delay cancellation the rectangular-pulse case shows only 1.8 dB improvement over the single-delay case. However, more realistic pulse representations show substantial improvement. The triangular and cosine representations have a rolloff of about 30 dB per decade; the smoother cosine-squared and gaussian representations roll off at 40 dB per decade.

## 16.10 EFFECT OF MULTIPLE SPECTRA

---

An airborne search-radar system may be operated at an altitude so that the radar horizon is approximately at the maximum range of interest. This results in sea or ground clutter being present at all ranges of interest. Other clutter sources such as rain and chaff may coexist with the surface clutter. In most instances these sources are moving at a speed determined by the mean wind aloft and have a mean doppler frequency significantly different from that of the surface clutter. If the MTI filter is tracking the surface clutter, the spectra of the sources with a different mean doppler frequency lie in the passband of the MTI filter. A 20-kn differential in an S-band system corresponds to 200 Hz, which would be at an optimum response in a 400-PRF system. A single-delay secondary canceler can be cascaded with either a single-delay or a double-delay primary canceler. The primary canceler tracks the mean surface velocity and rejects surface clutter. The single-delay canceler tracks the secondary source and rejects it. Since the pass and rejection bands of the two cancelers overlap, the MTI improvement factor for each clutter source is a function of their spectral separation.

Figure 16.29 shows the improvement factor for a double canceler which consists of two single cancelers, each tracking one of the spectra. It can be seen that, as the separation varies from 0 to one-half of the PRF, the performance degrades from that equivalent to a double canceler to the performance of a single canceler at half of the PRF.

The triple canceler has a double-delay canceler tracking the primary spectra and a single-delay canceler tracking the secondary spectra. The performance of the primary system varies from that of a triple canceler to a level less than that of a double canceler. The secondary-system performance varies from that of a triple canceler to a performance level lower than that of a single canceler.

## 16.11 DETECTION OF GROUND MOVING TARGETS

---

Vehicles and ships may have radial speeds that are significantly greater than the clutter velocity spectrum. This allows these targets to be detected. However, for an AEW system operating overland, ground traffic can saturate the tracking system. Furthermore, traffic density on major highways, target aspect changes causing strong scintillation, and shadowing by cultural features that occurs at low grazing angles can result in misassociation in the target-tracking system, causing false and runaway tracks. Runaway tracks are false tracks whose high speed causes them to rapidly move away from the true target position. They can associate with other reported positions or false alarms and thus perpetuate themselves. Since ground traffic is not of interest in the AEW case, these undesired targets are censored on the basis of highway grid maps, the small change in range during the antenna dwell, or the small velocity determined by a scan-to-scan processor or the tracking system. High-PRF pulse doppler radars use a low-frequency stopband filter to reject these velocity regions along with main-beam clutter. Low-PRF AEW radars bypass these censor circuits in the portion of the surveillance region that is over water. This allows slow-moving shipping targets to be detected.

Air-to-surface search radars, as well as airborne battlefield surveillance radars, are designed to maximize detection of slowly moving targets. Higher-

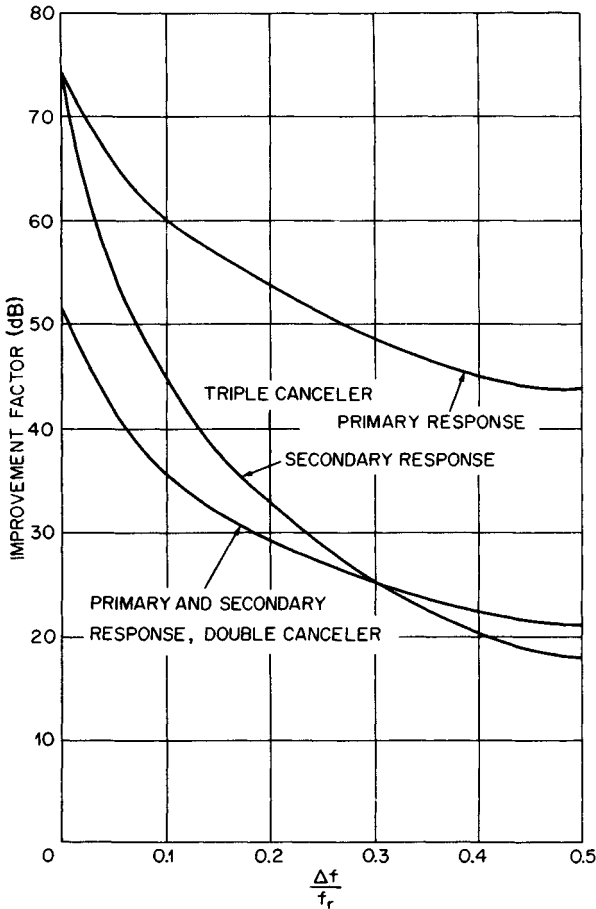


FIG. 16.29 MTI improvement factor for a double-notch canceler tracking two spectra as a function of the normalized spectra separation  $\Delta f/f_r$ . Normalized spectral width  $\sigma_c/f_r = 0.01$ .

frequency bands (X or K) are chosen to maximize the doppler shift. The PRF is chosen to optimize detection over the expected doppler frequency region of these targets. Since a strong clutter background is usually present, battlefield surveillance radars can effectively utilize noncoherent MTI techniques. However, the clutter spectrum is convolved with the target spectrum, which broadens the resultant target spectrum, thus widening the blind-speed zone and reducing doppler resolution. When the target phase coincides with the clutter phase, the targets are suppressed. In regions that are shadowed by hills or mountains, the targets are not detected.

Side-looking radars can produce a large number of pulses, thus increasing radar sensitivity. If a coherent radar is used, improved sensitivity and resolution can be obtained by using doppler filter banks or digital fast Fourier transform (FFT) processing. If the platform motion compared with the aperture length is sufficiently large, platform-motion compensation will be required.

Ship detection can be improved by rapidly scanning the antenna so that sea clutter is decorrelated and surface-target returns are integrated or leave a pattern of returns indicating their track. In some cases, frequency agility can also be utilized to decorrelate clutter and integrate ship target returns. Scan-to-scan video cancellation can be utilized for detecting moving targets overland if their scan-to-scan motion is of the order of the radar pulse width.

## REFERENCES

---

1. Emerson, R. C.: Some Pulsed Doppler MTI and AMTI Techniques, *Rand Corporation Rept. R-274, DDC Doc. AD 65881*, Mar. 1, 1954. (Reprinted in Ref. 6.)
2. George, T. S.: Fluctuations of Ground Clutter Return in Airborne Radar Equipment, *Proc. IEE (London)*, vol. 99, pt. IV, pp. 92-99, April 1952.
3. Dickey, F. R., Jr.: Theoretical Performance of Airborne Moving Target Indicators, *IRE Trans.*, vol. PGAE-8, pp. 12-23, June 1953.
4. Berkowitz, R. S. (ed.): "Modern Radar: Analysis, Evaluation and System Design," John Wiley & Sons, New York, 1966.
5. Barton, D. K.: "Radar Systems Analysis," Prentice-Hall, Englewood Cliffs, N.J., 1964.
6. Schlerer, D. C. (ed.): "MTI Radar," Artech House, Inc., Norwood, Mass., 1978.
7. Dickey, F. R., Jr., and M. M. Santa: Final Report on Anticlutter Techniques, *General Electric Company Rept. R65EMH37*, Mar. 1, 1953.
8. Anderson, D. B.: A Microwave Technique to Reduce Platform Motion and Scanning Noise in Airborne Moving Target Radar, *IRE WESCON Conv. Rec.*, vol. 2, pt. 1, pp. 202-211, 1958.
9. "Final Engineering Report on Displaced Phase Center Antenna," vol. 1, Mar. 26, 1956; vols. 2 and 3, Apr. 18, 1957, General Electric Company, Schenectady, N.Y.
10. Urkowitz, H.: The Effect of Antenna Patterns on Performance of Dual Antenna Radar Moving Target Indicators, *IEEE Trans.*, vol. ANE-11, pp. 218-223, December 1964.
11. Tsandoulis, G. N.: Tolerance Control in an Array Antenna, *Microwave J.*, pp. 24-35, October 1977.
12. Shroeder, K. G.: Beam Patterns for Phase Monopulse Arrays, *Microwaves*, pp. 18-27, March 1963.
13. Grissetti, R. S., M. M. Santa, and G. M. Kirkpatrick: Effect of Internal Fluctuations and Scanning on Clutter Attenuation in MTI Radar, *IRE Trans.*, vol. ANE-2, pp. 37-41, March 1955.
14. Andrews, G. A.: Airborne Radar Motion Compensation Techniques: Optimum Array Correction Patterns, *Naval Res. Lab. Rept. 7977*, Mar. 16, 1976.
15. Lopez, A. R., and W. W. Ganz: CPCT Antennas for AMTI Radar, vol. 2: Theoretical Study, *Air Force Avionics Lab. Rept. WL1630.22, AD 51858*, June 1970. (Not readily available.)
16. Brennan, L. E., J. D. Mallett, and I. S. Reed: Adaptive Arrays in Airborne MTI Radar, *IEEE Trans.*, vol. AP-24, pp. 607-615, September 1976.
17. Applebaum, S. P.: Adaptive Arrays, *IEEE Trans.*, vol. AP-24, pp. 585-598, September 1976.
18. Brennan, L. E., E. L. Pugh, and I. S. Reed: Control Loop Noise in Adaptive Array Antennas, *IEEE Trans.*, vol. AES-7, March 1971.
19. Monzingo, R. A., and T. W. Miller: "Introduction to Adaptive Arrays," John Wiley & Sons, New York, 1980.